Computationally Efficient Frequency Domain Method for Dynamic Control Derivative Estimation with Application to Transonic Truss-Braced Wing

Nhan Nguyen*
NASA Ames Research Center, Moffett Field, CA 94035
Juntao Xiong†
KBR Wyle, Inc., Moffett Field, CA 94035

This paper presents a computationally efficient method for dynamic control derivative estimation technique via control surface oscillation numerical experiments. Unsteady RANS CFD simulations in FUN3D are performed to simulate the control surface oscillations with a prescribed truncated square wave containing sufficient frequencies of interest. The truncated square wave oscillation offers the computational efficiency which reduces the computational cost by almost an order of magnitude compared to a sine wave oscillation. The nonlinear effect of large control surface oscillation amplitudes creates a spillover effect whereby the frequency response at the same input frequencies contains not only the linear aerodynamic response but also nonlinear aerodynamic response. A correction procedure is developed to remove the spillover effect from the linear aerodynamic response. A frequency-domain regression is performed to estimate the dynamic control derivatives after the correction. The results generally agree with the previous results obtained from the sine wave oscillation.

I. Introduction

Vehicle stability and control is an area of study that deals with the design and analysis aspects of aircraft stability and control. Vehicle stability requires that an aircraft design be statically and dynamically stable and controllable in all three axes of the motion in roll, pitch, and yaw. Vehicle control is accomplished by aerodynamic control surfaces or other control effectors.

A stability and control analysis is usually required to determine a set of stability and control derivatives with respect to the aircraft state and control variables. The stability and control derivatives include both steady state derivatives such as C_{m_α}, the pitching moment stability derivative with respect to the angle of attack, and $C_{m_{\delta_e}}$, the pitching moment control derivative with respect to the elevator deflection . Dynamic derivatives are the sensitivities evaluated by the partial derivatives with respect to the dynamic state variables of the aircraft such as the pitch rate q and control surface acceleration $\ddot{\delta}_e$. The dynamic stability derivatives with respect to the angular rates p, q, and r generally can be computed by some analytical techniques. On the other hand, dynamic derivatives with respect to the time derivatives of the aircraft state and control variables are more difficult to established. These derivatives account for the time delay in the aerodynamic response of the aircraft which can be important. The steady state and dynamic stability derivatives can be estimated experimentally by stability-and-control wind tunnel experiments or analytically by unsteady flow simulations.

The numerical estimation of dynamic stability and control derivatives is a current research topic. Recent work in this area can be found in many references.[1–3] Many of these technique do not adequately capture the various terms of the dynamic stability derivatives. More importantly, the effects of the frequency response on the dynamic stability derivatives is not well addressed especially for aircraft operating in transonic flight regime. Murman uses reduced-frequency approach to address the frequency response, but the approach lacks sufficient details to enable a systematic

*Senior Research Scientist and Technical Group Lead of Advanced Control and Engineering Systems Group, Intelligent Systems Division, nhan.t.nguyen@nasa.gov
†Aerospace Engineer, Intelligent System Division, juntao.xiong@nasa.gov

approach to determining the dynamic stability derivatives.[3] A frequency-domain dynamic stability estimation has recently been developed[4] and applied to the Mach 0.8 Transonic Truss-Braced Wing (TTBW) aircraft,[5] shown in Figure 1. Using unsteady RANS CFD simulation results, the time histories of the aerodynamic coefficients are transformed into the frequency domain by a Fourier series analysis as a function of the reduced frequency. A frequency-domain transfer function is designed to capture both the steady state and dynamic derivatives. The transfer function is formulated based on the Theodorsen's theory.[9] A frequency-domain regression analysis is then performed to estimate the transfer function. The proposed method can estimate those dynamic stability derivatives that are usually not captured in many analyses but do exist in the Theordorsen's theory such as $C_{m_{\dot{q}}}$ due to the apparent mass effect.

Figure 1. Boeing Mach 0.8 Transonic Truss-Braced Wing Aircraft Concept

This study continues the investigation of the stability and control estimation using high-fidelity CFD. In this study, we develop a frequency-domain estimation of the control derivatives for the TTBW taking into account significant nonlinearity in the aerodynamic response due to the large control surface deflections. In our prior work, the motion of the control surfaces is prescribed by a series of sine waves at various frequencies. In this study, the motion is prescribed by a truncated square wave with prescribed number of harmonics. This new method provides a larger frequency bandwidth in the frequency response than the sine wave oscillation at a much lower computational cost.

II. Control Derivative Estimation Method by Truncated Square Wave Oscillation

In our previous work, nonlinear control derivative estimation using the sine wave control surface oscillation has been developed.[9, 10] However, to accurately obtain the control derivatives, the aerodynamic response over a wide range of frequencies becomes necessarily. This involves using a large number of sine wave oscillations at varying discrete frequencies. The cost of running these unsteady CFD simulations can be prohibitively. In this work, we introduce an alternative forced oscillation method using a truncated square wave in order to reduce the computational cost associated with the sine wave oscillation. The truncated square wave oscillation can excite multiple frequencies all at once which can significantly decrease the computational cost.

When the amplitude δ_0 of the control surface oscillation is small, the flow is largely attached and linear. This greatly facilitates the estimation of stability and control derivatives. Since aerodynamic control surfaces are designed to operate over a large range of deflection angles, it is important to assess the nonlinear control effectiveness. While the use of the proposed truncated square wave oscillation provides computational efficiency, it also introduces complexity when the flow is nonlinear due to flow separation over a control surface at large deflection angles. In this study, we present a method for estimating the control effectiveness using a truncated square wave oscillation.

In our previous work,[9,10] a nonlinear model of the unsteady aerodynamic coefficient is proposed as

$$\tilde{C}_L = \sum_{n=1}^{N} \tilde{C}_{L_{\tilde{\delta}^n}}(\bar{s})\,\tilde{\delta}^n \tag{1}$$

where $\bar{s} = ik$, $k = \frac{\omega \bar{c}}{2V_\infty}$ is the reduced frequency, and $\tilde{C}_{L_{\tilde{\delta}^n}}(\bar{s})$ is the nonlinear unsteady aerodynamic transfer function which represents the control derivative with respect to the nonlinear deflection $\tilde{\delta}^n$.

In this study, we propose the control derivative in the form

$$\tilde{C}_{L_{\tilde{\delta}^n}}(\bar{s}) = \begin{cases} \dfrac{\sum_{p=0}^{l+2} e_{p1}\bar{s}^p}{\bar{s}^l + \sum_{p=0}^{l-1} b_{p1}\bar{s}^p} & n = 1 \\ \dfrac{\sum_{p=0}^{l} e_{pn}\bar{s}^p}{\bar{s}^l + \sum_{p=0}^{l-1} b_{p1}\bar{s}^p} & n \neq 1 \end{cases} \tag{2}$$

where the coefficients e_{pn} and b_{pn} are to be identified by a frequency-domain regression. The order of the numerator polynomial of $\tilde{C}_{L_{\tilde{\delta}}}(\bar{s})$ is two greater than that of the denominator polynomial to account for the derivatives with respect to the linear deflection rate $\frac{d\tilde{\delta}}{d\tau}$ and linear deflection acceleration $\frac{d^2\tilde{\delta}}{d\tau^2}$.

The system identification process involves applying a forced oscillation input to the aircraft and obtaining the aerodynamic response of the unsteady aerodynamic coefficient for the purpose of system identification. In this study, we consider a truncated square wave control surface oscillation represented by a Fourier sine series

$$\tilde{\delta} = \delta_0 \sum_{m=1,odd}^{M} \frac{1}{m} \sin mk_0\tau \tag{3}$$

where $\tau = \frac{2V_\infty}{\bar{c}}t$ is the nondimensional time and M is the number of harmonics in the Fourier sine series. In this work, we choose $k_0 = 0.02$ as the fundamental reduced frequency and $M = 25$ to capture the frequency response at 13 discrete frequencies in the reduced frequency range up to 0.5.

The unsteady aerodynamic coefficient is then expressed as a Fourier series

$$\tilde{C}_L = \sum_{n=1}^{N} (Q_{jn} + iS_{jn})\,\tilde{\delta}^n \tag{4}$$

where

$$\tilde{\delta}^n = \begin{cases} \sum_{j=1,odd}^{nM} \delta_0^n a_{jn} \sin k_j\tau & n \text{ odd} \\ \sum_{j=2,even}^{nM} \delta_0^n b_{jn} \cos k_j\tau & n \text{ even} \end{cases} \tag{5}$$

with $k_j = jk_0$.

The coefficients a_{jn} and b_{jn} are computed by a Fourier series analysis according to

$$a_{jn} = \frac{k_0}{N_P \pi \delta_0^n} \int_0^{\frac{2N_P\pi}{k_0}} \tilde{\delta}^n \sin k_j\tau\, d\tau \tag{6}$$

$$b_{jn} = \frac{k_0}{N_P \pi \delta_0^n} \int_0^{\frac{2N_P\pi}{k_0}} \tilde{\delta}^n \cos k_j\tau\, d\tau \tag{7}$$

where N_p is the number of periods in the time series data.

The Fourier series coefficients Q_{jn} and S_{jn} are computed as

$$Q_{jn} = \frac{k_0}{N_P \pi \delta_0^n a_{jn}} \int_0^{\frac{2N_P\pi}{k_0}} \tilde{C}_L \sin k_j\tau\, d\tau \tag{8}$$

$$S_{jn} = \frac{k_0}{N_P \pi \delta_0^n a_{jn}} \int_0^{\frac{2N_P\pi}{k_0}} \tilde{C}_L \cos k_j\tau\, d\tau \tag{9}$$

The linear aerodynamic response to the truncated square wave oscillation occurs at the frequencies $k_j = jk_0$, $j = 1, odd, \ldots, M$. However, the nonlinear aerodynamic response also occurs at the same frequencies. This creates a "spillover" effect on the linear aerodynamic response. The spillover effect causes a challenge in identifying the linear and nonlinear control derivatives. This issue has been identified in the previous work with the sine wave oscillation,[9, 10] but can be overcome with the method developed in the previous study. The truncated square wave creates a more complicated analysis issue. We provide one potential method for separating the linear aerodynamic response from the overall nonlinear aerodynamic response for large control surface oscillation amplitudes.

We note that the largest odd-power N_{odd} frequency response occurs at the frequencies k_j, $j = 1, odd, \ldots, N_{odd}M$. The non-overlapping frequencies occur at the frequencies k_j, $j = j = (N_{odd} - 2)M + 2, odd, \ldots, N_{odd}M$. Using these non-overlapping frequencies, a system identification can be performed to estimate the control derivative $\tilde{C}_{L_{\bar{\delta}^{N_{odd}}}}(\bar{s})$. The identified control derivative $\tilde{C}_{L_{\bar{\delta}^{N_{odd}}}}(\bar{s})$ is then used to predict the nonlinear aerodynamic response at the overlapping frequencies k_j, $j = 1, odd, \ldots, (N_{odd} - 2)M$. By subtracting off the nonlinear aerodynamic response of $\tilde{C}_{L_{\bar{\delta}^{N_{odd}}}}(\bar{s})$ from the overall aerodynamic response $\tilde{C}_{L_{\bar{\delta}^n}}(\bar{s})$, $n = 1, odd, \ldots, N_{odd} - 2$, at the overlapping frequencies, The frequency response $\tilde{C}_{L_{\bar{\delta}^n}}(\bar{s})$ can be obtained successively in stages whereby at each stage the correction procedure is applied to remove the overlapping frequency response from the next higher odd-power frequency response $\tilde{C}_{L_{\bar{\delta}^{n+2}}}(\bar{s})$. The procedure is repeated until $\tilde{C}_{L_{\bar{\delta}}}(\bar{s})$ is reached. The same procedure can be applied to the even-power control derivatives $\tilde{C}_{L_{\bar{\delta}^n}}(\bar{s})$, $n = 2, even, \ldots, N_{even}$, where $N = \max(N_{odd}, N_{even})$.

A frequency-domain regression is then performed to estimate the coefficients e_{pn} and b_{pn} of the control derivative $\tilde{C}_{L_{\bar{\delta}^n}}(\bar{s})$. In particular, for the linear control derivative $\tilde{C}_{L_{\bar{\delta}^n}}(\bar{s})$, after all the overlapping nonlinear frequency responses have been removed, the remaining unsteady aerodynamic coefficient due to the linear contribution is represented by

$$\Delta\tilde{C}_L = \sum_{j=1,odd}^{M} \frac{\sum_{p=0}^{l+2} e_{p1} i^p k_j^p \delta_0 a_{j1} \sin k_j \tau}{i^l k_j^l + \sum_{p=0}^{l-1} b_{p1} i^p k_j^p} \tag{10}$$

The linear control derivative is then obtained as

$$\tilde{C}_{L_{\bar{\delta}}}(ik_j) = \frac{\sum_{p=0}^{l+2} e_{p1} i^p k_j^p}{i^l k_j^l + \sum_{p=0}^{l-1} b_{p1} i^p k_j^p} = Q_{j1} + iS_{j1} \tag{11}$$

Thus, a frequency-domain regression can be performed to compute e_{p1} and b_{p1}. This is a minimization problem with the following cost function:

$$J = \frac{1}{2}\left|\sum_{p=0}^{l+2} e_{p1} i^p k_j^p - \left(i^p k_j^l + \sum_{p=0}^{l-1} b_{p1} i^p k_j^p\right)\left(Q_{1j} + iS_{1j}\right)\right| \tag{12}$$

This minimization leads to a matrix equation which can be solved for e_{p1} and b_{p1}.

III. Application to Transonic Truss-Braced Wing

The truncated square wave oscillation method is applied to the Mach 0.8 TTBW for the dynamic control derivative estimation. Figure 2 illustrates control surface layout for the Mach 0.8 TTBW.[7]

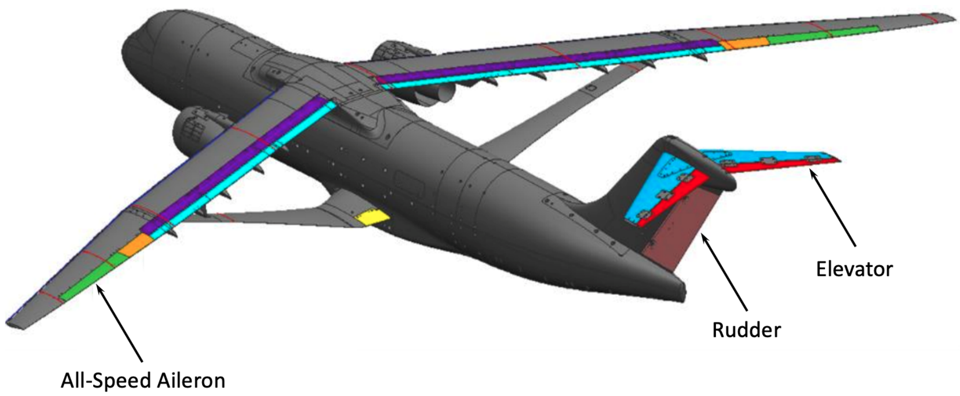

Figure 2. Control Surface Layout of Mach 0.8 Transonic Truss Braced-Wing

A series of unsteady RANS CFD simulations of the control surface oscillations of the elevator, outboard all-speed aileron, and rudder of the Mach 0.8 TTBW is conducted in FUN3D.[8] The individual elevator control surfaces are modeled as a single control surface in symmetric deflections. The individual outboard all-speed aileron control surfaces are modeled as a single control surface in anti-symmetric deflections. The FUN3D tetrahedral prism mesh has about 96 million nodes. The Roe's flux-difference splitting scheme and the Spalart-Allmaras turbulence model are used in the simulations. An optimized second-order backward finite-difference scheme is used in the time integration.

A. Elevator Dynamic Control Derivative Estimation

The elevator control surface oscillation is simulated by two truncated square waves of 1° and 20° amplitudes, each with 13 harmonics or $M = 25$ in the reduced frequency range from $k_0 = 0.02$ to $k_{max} = Mk_0 = 0.5$. Figure 3(a) shows the pressure contour plots for the 20° amplitude. Shock-induced boundary layer separation at the hinge line is observed. Figure 3(b) shows the pressure distribution on a horizontal tail section with the 20° amplitude. The pressure distribution indicates a flow separation region on the entire elevator control surface.

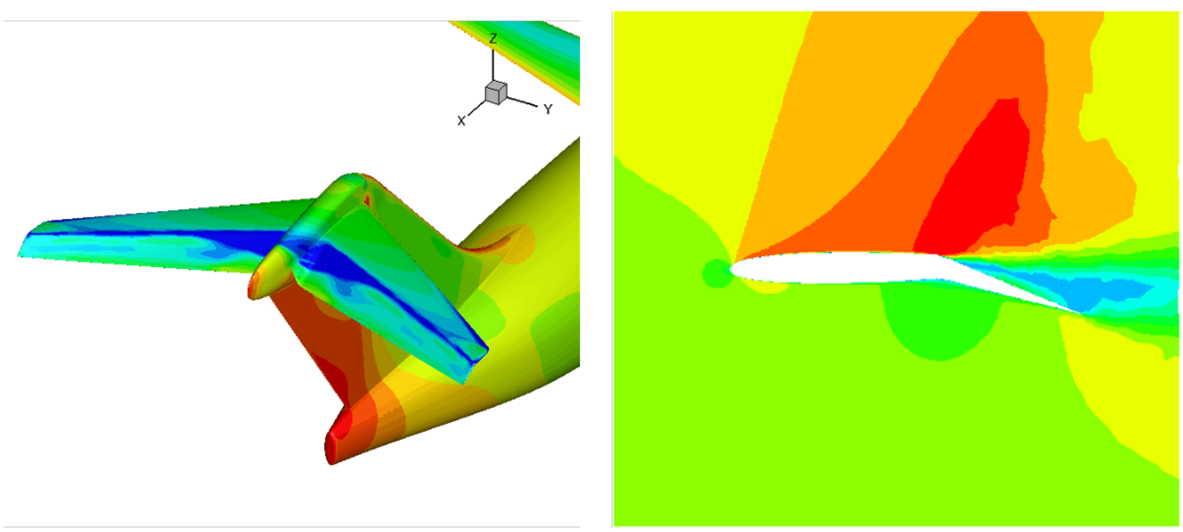

(a) (b)

Figure 3. Instantaneous Pressure Contour Due to Elevator Deflection for 20° Amplitude

The plots of the time histories of the the unsteady lift and pitching moment coefficients for the last period of the converge solution for the 1° amplitude are shown in Figs. 4(a) and (b), respectively. At small amplitudes, the frequency responses of the lift and pitching moment coefficients are predominantly linear

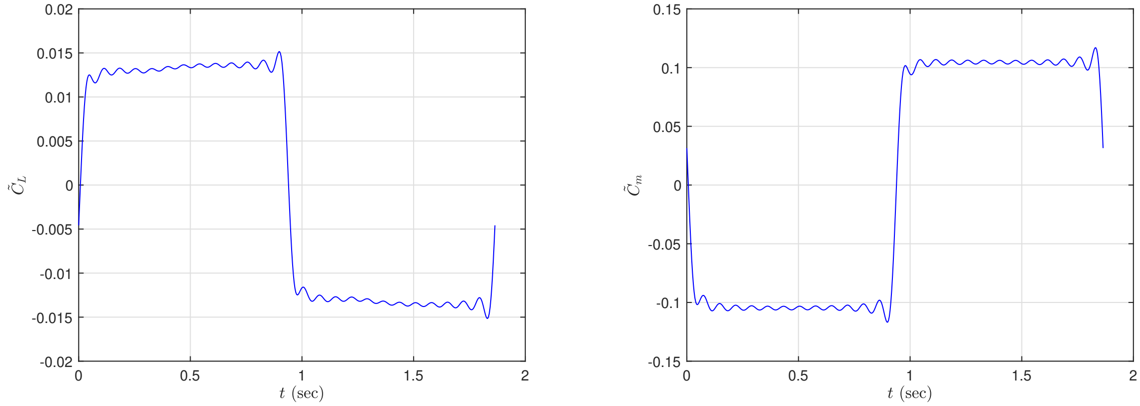

(a) $\tilde{C}_L$ (b) $\tilde{C}_m$

Figure 4. Time Histories of Elevator Deflection and Lift, Pitching Moment, and Drag Coefficients for 1° Amplitude

The lift control derivative of the elevator is modeled by the following transfer function

$$\tilde{C}_{L_{\tilde{\delta}_e}}(\bar{s}) = \left(1 + \frac{a_1 \bar{s}}{\bar{s}^2 + b_1 \bar{s} + b_0}\right)(c_0 + c_1 \bar{s}) + d_1 \bar{s} + d_2 \bar{s}^2 \tag{13}$$

The steady-state and dynamic control derivatives are obtained as

$$C_{L_{\delta_e}} = c_0 \tag{14}$$

$$C_{L_{\dot{\delta}_e}} = c_1 + d_1 \tag{15}$$

$$C_{L_{\ddot{\delta}_e}} = d_2 \tag{16}$$

The quantities c_0 and c_1 are the circulatory control derivatives, whereas the quantities d_1 and d_2 are the apparent-mass contributions to the dynamic control derivatives.

Figures 5(a) and (b) show the frequency-domain regression of the lift and pitching moment control derivatives, respectively, for the 1° amplitude. The plots show the frequency responses extracted for the first 13 harmonics. The results are also compared to those obtained previously from CFD simulations of the sine wave oscillation at three discrete reduced frequencies of 0.02, 0.1, and 0.2.[9,10] The frequency responses of the lift and pitching moment control derivatives obtained from the truncated square wave oscillation match very well those obtained from the sine wave oscillation.

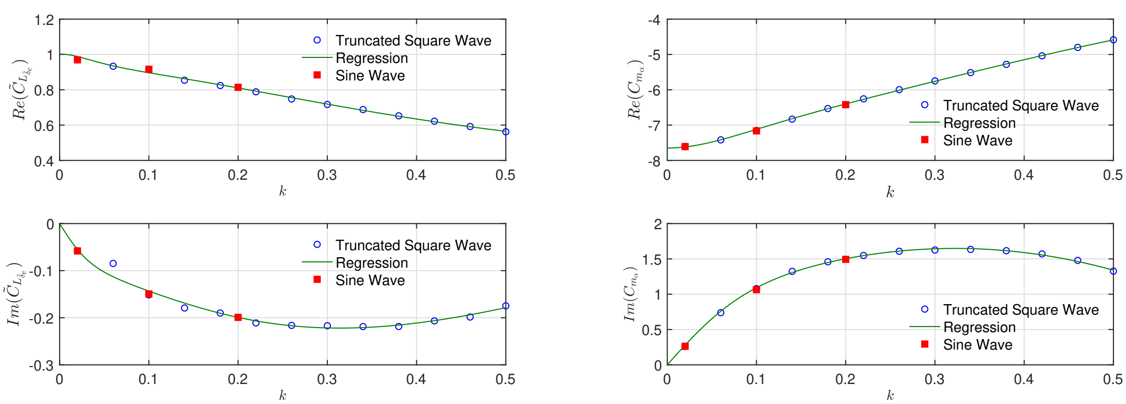

(a) $\tilde{C}_{L_{\tilde{\delta}_e}}$ (b) $\tilde{C}_{m_{\tilde{\delta}_e}}$

Figure 5. Frequency-Domain Regression of Lift and Pitching Moment Control Derivatives of Elevator for 1° Amplitude

The lift and pitching moment control derivatives for the 1° amplitude are obtained from the frequency-domain regression to be

$$\tilde{C}_{L_{\tilde{\delta}_e}}(\bar{s}) = \left(1 - \frac{0.08259\bar{s}}{\bar{s}^2 + 0.5296\bar{s} + 0.02470}\right)(1.0022 + 9.5564\bar{s}) - 9.2033\bar{s} - 0.08410\bar{s}^2$$

$$\tilde{C}_{m_{\tilde{\delta}_e}}(\bar{s}) = \left(1 - \frac{0.3401\bar{s}}{\bar{s}^2 + 1.0005\bar{s} + 0.1186}\right)(-7.6489 - 37.0719\bar{s}) + 29.2406\bar{s} + 3.6773\bar{s}^2$$

The plots of the time histories of the elevator deflection and the unsteady lift and pitching moment coefficients for the 20° amplitude are shown in Figs. 6(a), (b), (c) and (d), respectively. The frequency responses of the lift and pitching moment coefficients are expected to be nonlinear due to the massive flow separation.

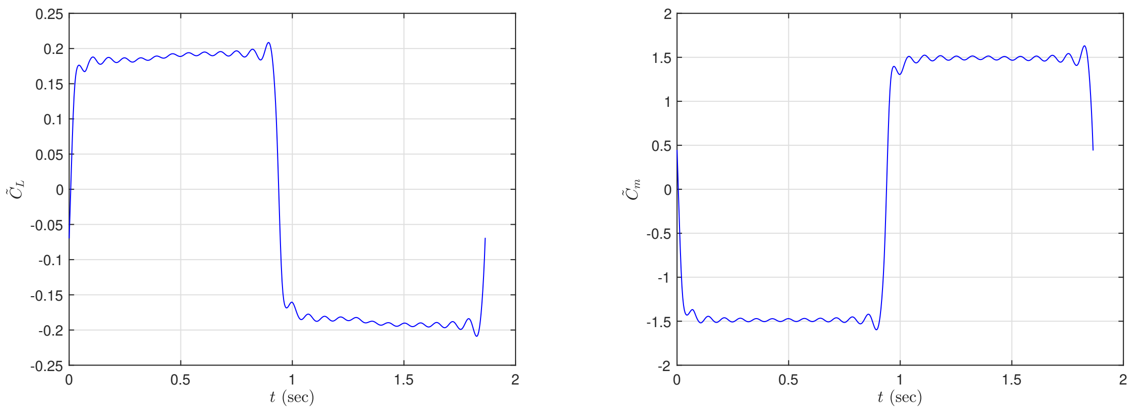

(a) $\tilde{C}_L$ (b) $\tilde{C}_m$

Figure 6. Time Histories of Lift and Pitching Moment Coefficients for 20° Amplitude

From the frequency spectra of the unsteady lift and pitching moment coefficients shown in Figures 7(a) and (b), a third-order nonlinearity is present in the data which appears as odd harmonics from $M + 2 = 27$ to $3M = 75$. There is also a second-order nonlinearity which appears as even harmonics from 2 to $2M = 50$. Higher-order nonlinearity beyond the third order is also present, but the contribution is relatively minor compared to the second- and third-order nonlinearity. The second-order nonlinearity does not interfere with the odd harmonics of the linear frequency response, but the third-order nonlinearity does. This interference creates a spillover effect which results in a reduction in the frequency response magnitude.

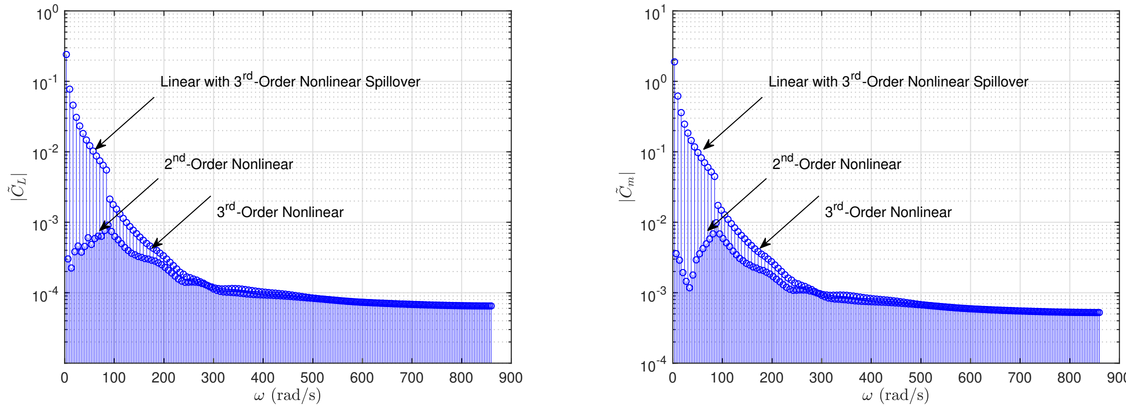

(a) $\tilde{C}_L$ (b) $\tilde{C}_m$

Figure 7. Frequency Spectra of Lift and Pitching Moment Coefficients for 20° Amplitude

The third-order nonlinear control derivative is estimated by performing a frequency-domain regression of the odd harmonics from $M+2$ to $3M$. These harmonics are non-overlapping and therefore can be easily handled. The third-order contribution by these harmonics is modeled as

$$\tilde{C}_{L_{\bar{\delta}^3}}(\bar{s}) = \left(1 + \frac{a_1 \bar{s}}{\bar{s}^2 + b_1 \bar{s} + b_0}\right) c_0$$

Figures 8(a) and (b) show the frequency-domain regression of the lift and pitching moment third-order control derivatives, respectively, for the 20° amplitude. The large magnitudes in the frequency responses are due to the Fourier coefficients a_{jn} tending to zero as the reduced frequency increases.

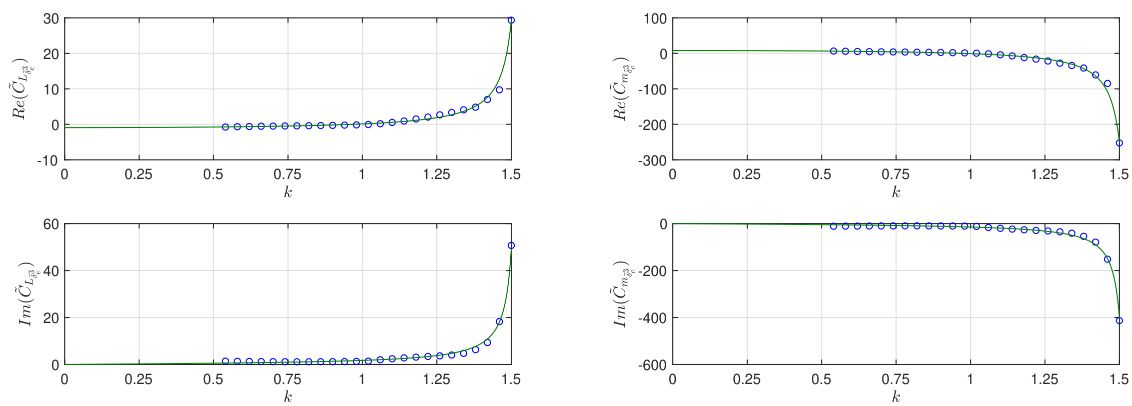

(a) $\tilde{C}_L$ (b) $\tilde{C}_m$

Figure 8. Frequency-Domain Regression of Lift and Pitching Moment 3^{rd}-Order Nonlinear Control Derivatives for 20° Amplitude

The regression yields

$$\tilde{C}_{L_{\bar{\delta}^3}}(\bar{s}) = \left(1 + \frac{1.5240\bar{s}^2 - 2.4915\bar{s}}{\bar{s}^2 - 0.01053\bar{s} + 2.3302}\right)(-0.9266)$$

$$\tilde{C}_{m_{\bar{\delta}^3}}(\bar{s}) = \left(1 + \frac{1.4922\bar{s}^2 - 2.4405\bar{s}}{\bar{s}^2 - 0.009394\bar{s} + 2.3317}\right)7.9548$$

The regression creates unstable poles at around $k = 1.5$ due to the large magnitudes. Therefore, the third-order nonlinear control derivatives are not useful at high reduced frequencies above $k = 1$. At low reduced frequencies, the third-order nonlinear control derivatives may be approximated by their steady-state values which are $C_{L_{\delta^3}} = -0.9266$ and $C_{m_{\delta_e^3}} = 7.9548$. In our previous work with the sine wave oscillation, the steady-state third-order nonlinear control derivatives are obtained to be $C_{L_{\delta^3}} = -2.840$ and $C_{m_{\delta_e^3}} = 22.68$.[10] This suggests that the proposed method to extract nonlinear control derivatives from a truncated square wave oscillation yields less than satisfactory results.

Using the third-order nonlinear control derivatives $\tilde{C}_{L_{\tilde{\delta}^3}}(\bar{s})$ and $\tilde{C}_{m_{\tilde{\delta}^3}}(\bar{s})$, the frequency responses at the odd harmonics from 1 to M where the linear frequency response occurs are computed. The frequency response at these harmonics includes the contribution from the third-order nonlinear frequency response which is expressed as

$$Q_{j1} + iS_{j1} = \frac{\sum_{p=0}^{l+2} e_{p1} i^p k_j^p}{i^l k_j^l + \sum_{p=0}^{l-1} b_{p1} i^p k_j^p} + \frac{\sum_{p=0}^{l} e_{p3} i^p k_j^p \frac{\delta_0^3 a_{j3}}{\delta_0 a_{j1}}}{i^2 k_j^2 + \sum_{p=0}^{l-1} b_{p3} i^p k_j^p} \tag{17}$$

By subtracting off the nonlinear frequency response at these harmonics, the linear frequency response should be recovered in theory. This is expressed as

$$\tilde{C}_{L_{\tilde{\delta}_e}}(ik_j) = Q_{j1} + iS_{j1} - \frac{\sum_{p=0}^{l} e_{p3} i^p k_j^p \frac{\delta_0^3 a_{j3}}{\delta_0 a_{j1}}}{i^2 k_j^2 + \sum_{p=0}^{l-1} b_{p3} i^p k_j^p} = \frac{\sum_{p=0}^{l+2} e_{p1} i^p k_j^p}{i^l k_j^l + \sum_{p=0}^{l-1} b_{p1} i^p k_j^p} \tag{18}$$

Figures (a) and (b) show the frequency-domain regression of the lift and pitching moment linear control derivatives, respectively, for the 20° amplitude. Both the corrected and uncorrected values are shown. The corrected values are with the nonlinear spillover effect removed for the regression analysis. Without the correction, the magnitudes of the control derivatives are smaller. Even with the correction, the linear control derivatives do not match those obtained for the 1° amplitude. This is not unexpected because the nonlinear behavior is not global, that is, it occurs only when a control surface deflection exceeds a certain amplitude. The nonlinear behavior is more aptly modeled as a piecewise nonlinear function, whereas the model used in the control derivative analysis assumes a global nonlinear function.

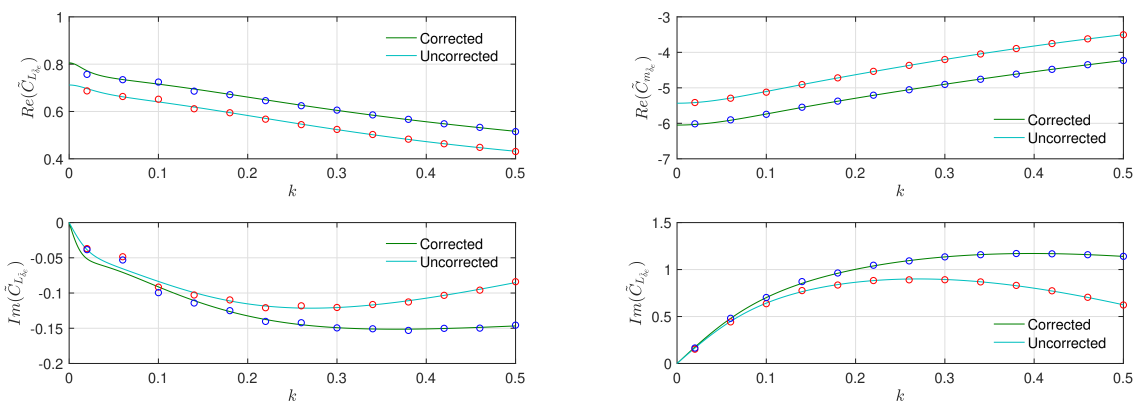

(a) $\tilde{C}_L$ (b) $\tilde{C}_m$

Figure 9. Frequency-Domain Regression of Lift and Pitching Moment Linear Control Derivatives for 20° Amplitude

The lift and pitching moment linear control derivatives for the 20° amplitude are

$$\tilde{C}_{L_{\tilde{\delta}_e}}(\bar{s}) = \left(1 - \frac{0.03578\bar{s}}{\bar{s}^2 + 0.3541\bar{s} + 0.007149}\right)(0.8055 + 9.2906\bar{s}) - 9.3356\bar{s} + 0.1505\bar{s}^2$$

$$\tilde{C}_{m_{\tilde{\delta}_e}}(\bar{s}) = \left(1 - \frac{0.1171\bar{s}}{\bar{s}^2 + 0.6863\bar{s} + 0.07633}\right)(-6.0495 - 26.3889\bar{s}) + 25.9159\bar{s} - 0.3622\bar{s}^2$$

Comparing the steady-state control derivatives $C_{L_{\delta_e}}$ and $C_{m_{\delta_e}}$, the lift control effectiveness of the elevator decreases by 20% and the pitch control effectiveness decreases by 21% as the elevator deflection increases from 1° to 20°.

B. Aileron Dynamic Control Derivative Estimation

The aileron control surface oscillation is simulated by two truncated square waves of 1° and 20° amplitudes with the same discrete frequencies as those for the elevator. The left and right aileron control surfaces are modeled as a single unit deflected in an anti-symmetric motion for roll control. Figure 10(a) shows the instantaneous pressure contour of the flow over the right wing with the right aileron deflected at 20°. Figure 10(b) shows a 2D pressure contour illustrated on a generic supercritical airfoil indicating a shock-induced flow separation at the hinge line.

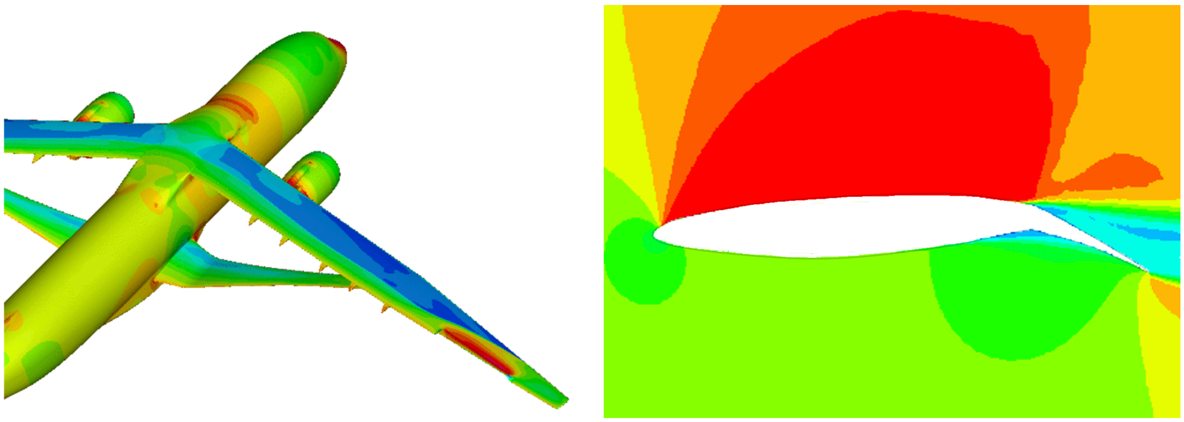

(a) (b)

Figure 10. Instantaneous Pressure Contour Due to Right Aileron Deflection at 20°

The frequency responses of the side force, rolling moment, and yawing moment control derivatives for the 1° and 20° amplitudes are shown in Figures 11(a)-(b), 12(a)-(b), and 13(a)-(b), respectively. The frequency responses of the side force and yawing moment show some scatter in the low reduced frequency ranges below 0.3. The control derivatives for the 1° amplitude are assumed to be due to mostly linear flow. Their magnitudes are generally higher than the magnitudes of the control derivatives for the 20° amplitude after corrections have been applied to remove the nonlinear spillover effect.

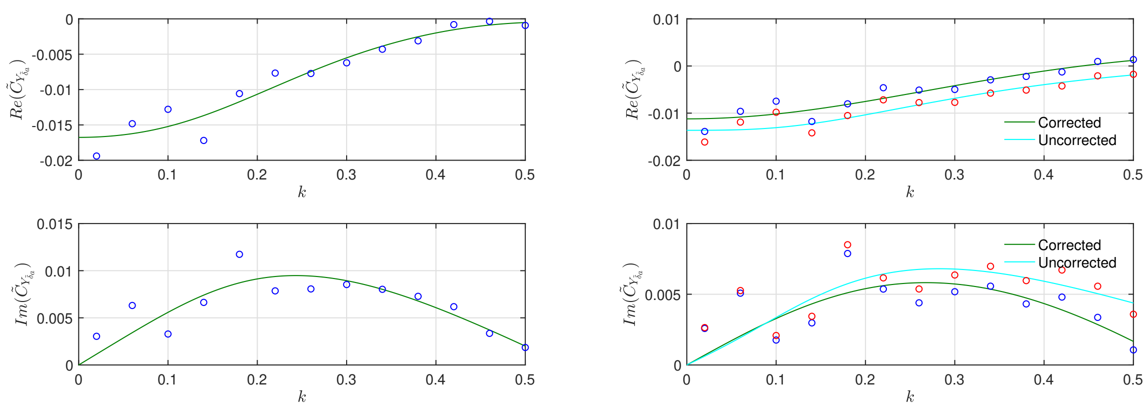

(a) 1° Amplitude (b) 20° Amplitude

Figure 11. Frequency-Domain Regression of Side Force Linear Control Derivatives of Aileron

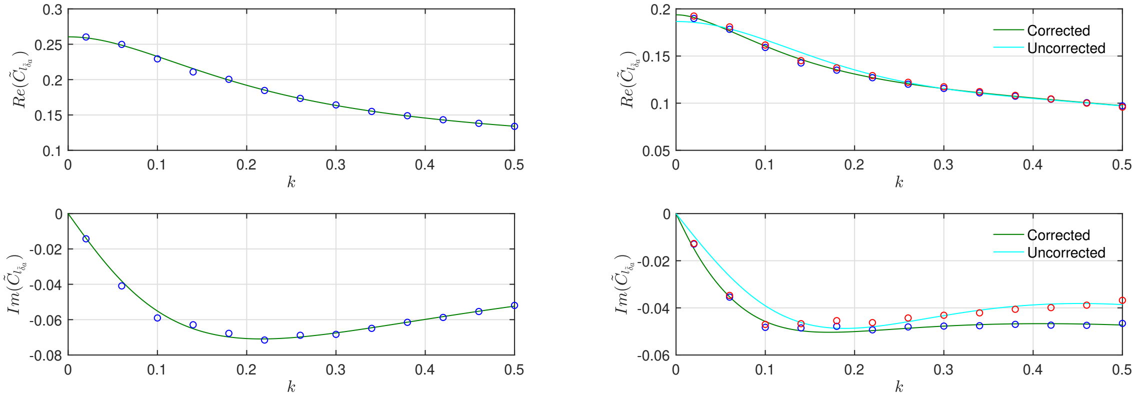

(a) 1° Amplitude (b) 20° Amplitude

Figure 12. Frequency-Domain Regression of Rolling Moment Linear Control Derivatives of Aileron

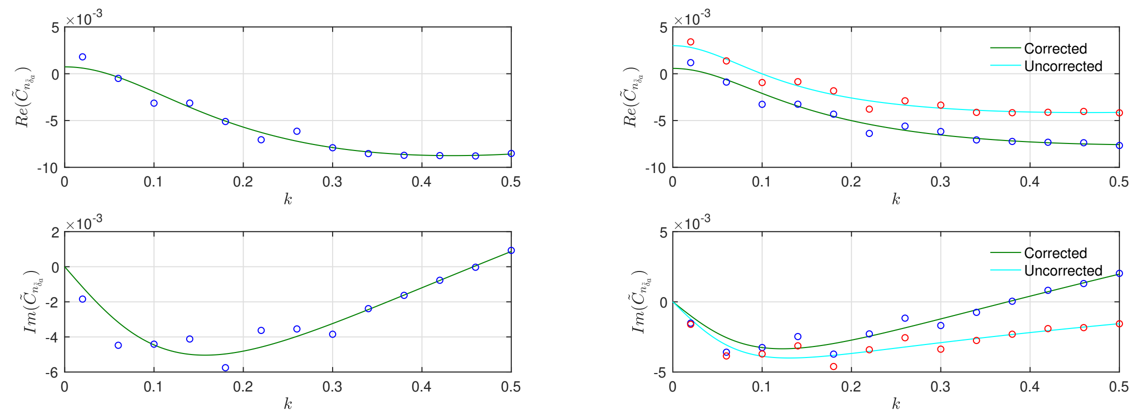

(a) 1° Amplitude (b) 20° Amplitude

Figure 13. Frequency-Domain Regression of Yawing Moment Linear Control Derivatives of Aileron

The linear control derivatives of the aileron for the 1° amplitude obtained from the frequency-domain regression are

$$\tilde{C}_{Y_{\tilde{\delta}_a}}(\bar{s}) = \left(1 - \frac{0.3897\bar{s}}{\bar{s}^2 + 0.54464\bar{s} + 0.07339}\right)(-0.01676 - 0.09227\bar{s}) + 0.06074\bar{s} + 0.02908\bar{s}^2$$

$$\tilde{C}_{l_{\tilde{\delta}_a}}(\bar{s}) = \left(1 - \frac{0.06701\bar{s}}{\bar{s}^2 + 0.3369\bar{s} + 0.02481}\right)(0.2605 + 2.1591\bar{s}) - 2.1595\bar{s} + 0.01948\bar{s}^2$$

$$\tilde{C}_{n_{\tilde{\delta}_a}}(\bar{s}) = \left(1 - \frac{5.9915\bar{s}}{\bar{s}^2 + 0.5175\bar{s} + 0.06110}\right)(0.0007359 + 0.002620\bar{s}) + 0.01079\bar{s} - 0.01386\bar{s}^2$$

The steady-state control derivatives of the aileron for the 1° amplitude are $C_{Y_{\delta_a}} = -0.01676$, $C_{l_{\delta_a}} = 0.2605$, and $C_{n_{\delta_a}} = 0.0007359$.

The linear control derivatives of the aileron for the 20° amplitude upon correction for the nonlinear spillover effect are

$$\tilde{C}_{Y_{\tilde{\delta}_a}}(\bar{s}) = \left(1 - \frac{2.6082\bar{s}}{\bar{s}^2 + 1.3308\bar{s} + 0.4427}\right)(-0.01121 - 0.01250\bar{s}) - 0.01852\bar{s} + 0.01837\bar{s}^2$$

$$\tilde{C}_{l_{\tilde{\delta}_a}}(\bar{s}) = \left(1 - \frac{0.02271\bar{s}}{\bar{s}^2 + 0.1852\bar{s} + 0.005989}\right)(0.1937 + 3.8984\bar{s}) - 3.9485\bar{s} + 0.05662\bar{s}^2$$

$$\tilde{C}_{n_{\tilde{\delta}_a}}(\bar{s}) = \left(1 - \frac{5.0830\bar{s}}{\bar{s}^2 + 0.4760\bar{s} + 0.04697}\right)(0.0005704 + 0.002106\bar{s}) + 0.008841\bar{s} - 0.003735\bar{s}^2$$

The steady-state control derivatives of the aileron for the 20° amplitude are $C_{Y_{\delta_a}} = -0.01121$, $C_{l_{\delta_a}} = 0.1937$, and $C_{n_{\delta_a}} = 0.0005704$. The roll control effectiveness of the aileron decreases by 27% as the aileron deflection increases from 1° to 20°. The side force and yaw control effectiveness of the aileron are generally small.

C. Rudder Dynamic Control Derivative Estimation

The rudder control surface oscillation is simulated with two truncated square waves with 1° and 10° amplitudes with the same discrete frequencies as those for the elevator. The rudder control surface is modeled using a blended mesh for the gap area. Figure 14(a) shows the instantaneous pressure contour with the rudder deflected at 10°. Figure 14(b) shows the pressure distribution on a vertical tail section which indicates a small shock at the hinge line, but the flow appears to be predominantly attached.

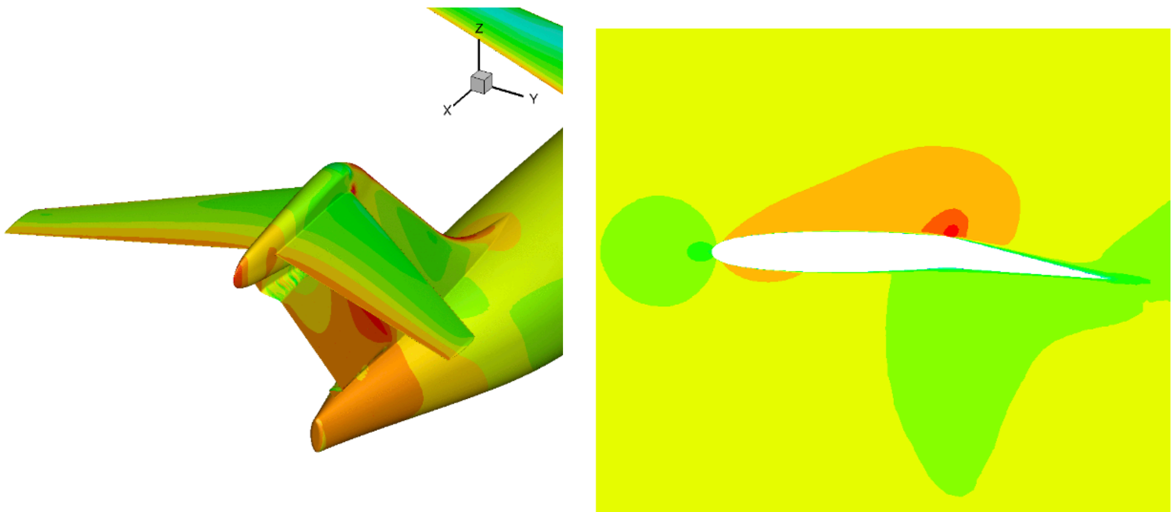

(a) (b)

Figure 14. Pressure Distribution with Rudder Deflection at 10°

The frequency responses of the side force, rolling moment, and yawing moment control derivatives for the 1° and 10° amplitudes are shown in Figures 15(a)-(b), 16(a)-(b), and 17(a)-(b), respectively. The frequency response of the rolling moment exhibits a significant amount of scatter which could be due to the low magnitude of the rolling moment.

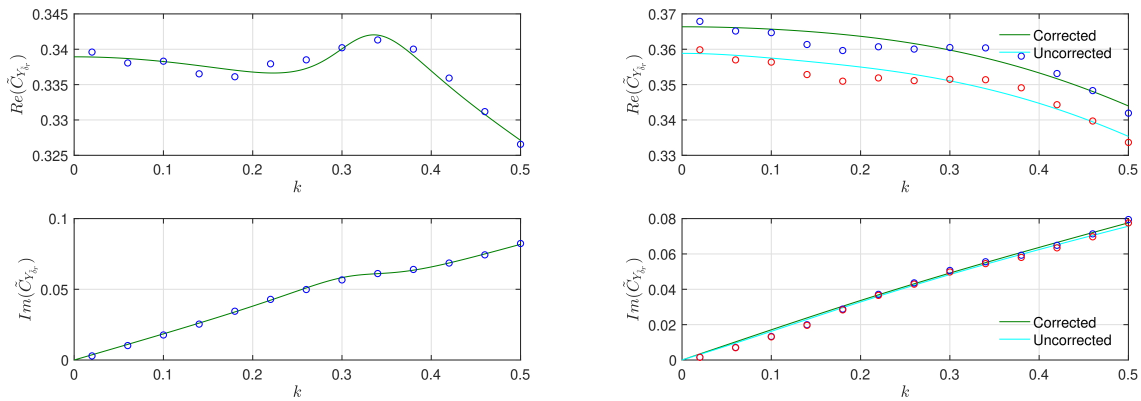

(a) 1° Amplitude

(b) 10° Amplitude

Figure 15. Frequency-Domain Regression of Side Force Linear Control Derivatives of Rudder

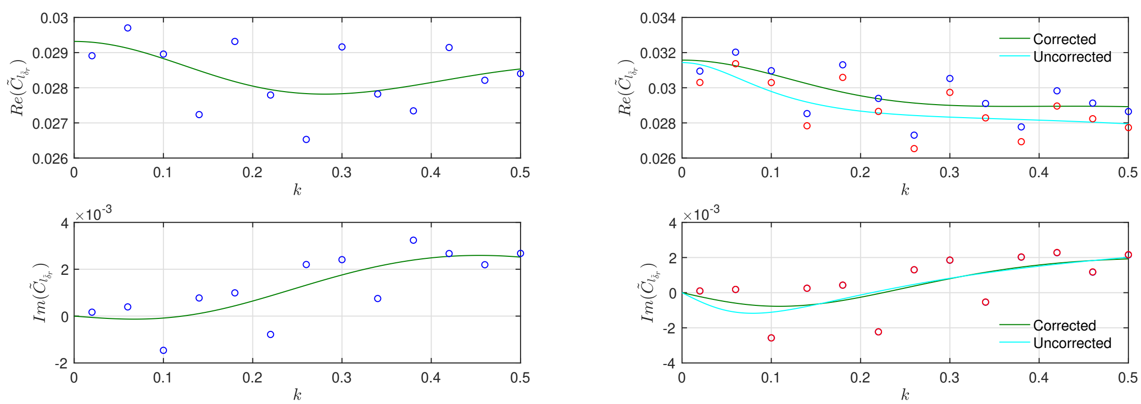

(a) 1° Amplitude

(b) 20° Amplitude

Figure 16. Frequency-Domain Regression of Rolling Moment Linear Control Derivatives of Rudder

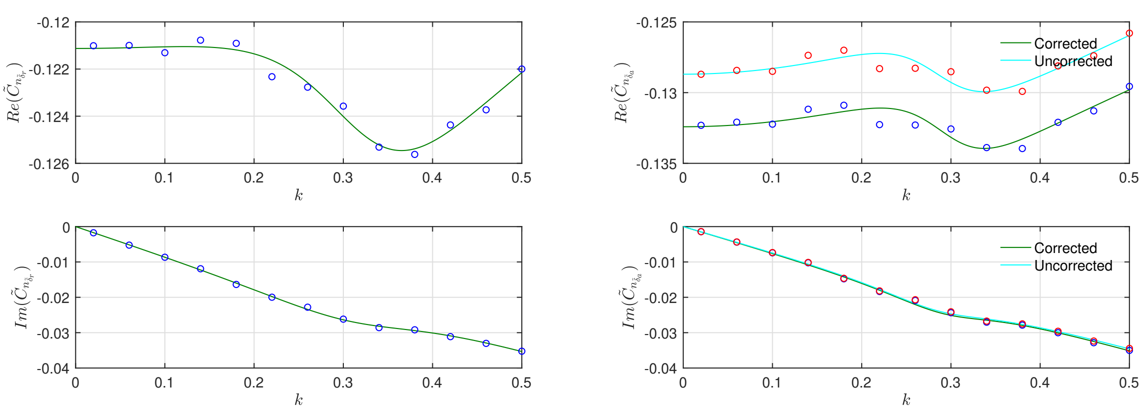

(a) 1° Amplitude

(b) 20° Amplitude

Figure 17. Frequency-Domain Regression of Yawing Moment Linear Control Derivatives of Rudder

The linear control derivatives for the 1° amplitude obtained from the frequency-domain regression are

$$\tilde{C}_{Y_{\tilde{\delta}_r}}(\bar{s}) = \left(1+\frac{0.00460424\bar{s}}{\bar{s}^2+0.1483\bar{s}+0.1092}\right)(0.3389+0.4676\bar{s})-0.2984\bar{s}+0.06836\bar{s}^2$$

$$\tilde{C}_{l_{\tilde{\delta}_r}}(\bar{s}) = \left(1+\frac{0.06394\bar{s}}{\bar{s}^2+0.8842\bar{s}+0.1923}\right)(0.02932+0.2569\bar{s})-0.2696\bar{s}+0.01948\bar{s}^2$$

$$\tilde{C}_{n_{\tilde{\delta}_r}}(\bar{s}) = \left(1+\frac{0.01327\bar{s}}{\bar{s}^2+0.2530\bar{s}+0.1202}\right)(-0.1211-0.1827\bar{s})+0.1104\bar{s}-0.01786\bar{s}^2$$

The steady-state control derivatives for the 1° amplitude are $C_{Y_{\delta_r}} = 0.3389$, $C_{l_{\delta_r}} = 0.02932$, and $C_{n_{\delta_r}} = -0.1211$. The linear control derivatives for the 10° amplitude upon correction for the nonlinear spillover effect are

$$\tilde{C}_{Y_{\tilde{\delta}_r}}(\bar{s}) = \left(1+\frac{0.009317\bar{s}}{\bar{s}^2+0.6584\bar{s}+0.1076}\right)(0.3664+1.6108\bar{s})-1.4710\bar{s}+0.008731\bar{s}^2$$

$$\tilde{C}_{l_{\tilde{\delta}_r}}(\bar{s}) = \left(1-\frac{0.03504\bar{s}}{\bar{s}^2+0.6982\bar{s}+0.1196}\right)(0.03157-0.1122\bar{s})+0.1101\bar{s}+0.05662\bar{s}^2$$

$$\tilde{C}_{n_{\tilde{\delta}_r}}(\bar{s}) = \left(1+\frac{0.003740\bar{s}}{\bar{s}^2+0.1575\bar{s}+0.09353}\right)(-0.1324-0.5389\bar{s})+0.4687\bar{s}-0.02327\bar{s}^2$$

The steady-state control derivatives for the 10° amplitude are $C_{Y_{\delta_r}} = 0.3664$, $C_{l_{\delta_r}} = 0.03157$, and $C_{n_{\delta_r}} = -0.1324$. The yaw control effectiveness of the rudder is about 9% larger than that for the 1° amplitude. This result is not expected and will be further investigated.

IV. Discussion

The proposed truncated square wave oscillation method offers a computationally efficient method in CFD simulations of forced oscillation numerical experiments for flight vehicle stability and control analysis. To accurately perform system identification of stability and control characteristics of a flight vehicle, the frequency responses of the aerodynamic forces and moments should be established over a wide range of discrete frequencies. This allows accurate estimation of stability and control derivatives by means of frequency-domain regression. Sine wave oscillation provides the highest level of energy at the same amplitude compared to any other oscillation methods, but the disadvantage with this method is that the computational cost of generating a reasonable set of discrete frequencies can be prohibitive. The truncated square wave oscillation overcomes this disadvantage by providing an oscillation signal with multiple input frequencies.

Table 1 presents the CPU time of the control surface oscillation simulations of the TTBW using the sine wave oscillation at discrete frequencies and the truncated square wave oscillation. The CPU time for each sine wave forced oscillation simulation is about 120 hours,[9,10] whereas the CPU time for the truncated square wave with 13 frequencies is 200 hours, or 15.4 hours per frequency. The CPU time per frequency with the truncated square wave oscillation is almost 8 times lower than that with the sine wave oscillation. Thus, the truncated square wave oscillation provides a wider frequency range at a much lower cost than the sine wave oscillation.

	Number of Frequencies	Frequency Range	Total CPU Hours	CPU Hour/Frequency
Sine Wave	3	0.02 – 0.2	360	120
Truncated Square Wave	13	0.02 – 0.5	200	15.4

Table 1. CPU Time Comparison Between Sine Wave and Truncated Square Wave Forced Oscillations

The advantage of the truncated square wave oscillation is generally offset by the reduced oscillation amplitude as the frequency increases. The low level of the oscillation amplitude could result in less accurate frequency response. Thus, there is a trade-off between the computational efficiency and the accuracy of the frequency response for stability and control derivative estimation. Moreover, the truncated square wave oscillation method generally presents more difficulty for nonlinear stability and control analysis than the sine wave oscillation, as illustrated in the current study.

V. Conclusions

A proposed truncated square wave oscillation is proposed as a computationally efficient method for CFD simulations of forced oscillation numerical experiments for flight vehicle stability and control analysis. The method can offer almost an order of magnitude reduction in the computational cost compared to the sine wave oscillation for the same number of input frequencies. For large amplitude forced oscillations, the resulting nonlinearity can cause difficulty with the truncated square wave method. A correction method is developed to remove the spillover effect of the nonlinearity from the frequency response at the input frequencies. A control derivative analysis is performed for the Transonic Truss-Braced Wing. The control derivatives obtained from this method generally agree with the previous control derivatives obtained by the sine wave oscillation. The nonlinear elevator control derivatives are significant smaller than those previously obtained by the sine wave method. There is a significant amount of scatter in the frequency response of the rolling moment to the rudder input. Further examination of the truncated square wave oscillation data will be performed to potentially improve the analysis method.

Acknowledgment

The authors wish to acknowledge NASA Advanced Air Transport Technology project for the funding support of this work. The authors also acknowledge Boeing Research and Technology and in particular Christopher Droney, Neal Harrison, Michael Beyar, Eric Dickey, and Anthony Sclafani, along with the NASA technical POC, Gregory Gatlin, for their research conducted under the NASA BAART contracts NNL10AA05B and NNL16AA04B. The research published in this paper is made possible by the technical data and wind tunnel test data furnished under these BAART contracts.

References

[1] Wang, F., and Chen, L., "Numerical Prediction of Stability Derivatives for Complex Configurations," Procedia Engineering 99 (2015) 1561-1575.

[2] Ghoreyshi M., Bergeron K., Lofthouse, A., and Cummings R., "CFD Calculation of Stability and Control Derivatives For Ram-Air Parachutes," AIAA Applied Aerodynamics Conference, AIAA-2016-1536, 2016.

[3] Murmann, S., "A Reduced-Frequency Approach for Calculating Dynamic Derivatives," AIAA Aerospace Sciences Meeting, AIAA-2005-0840, 2005.

[4] Nguyen, N. and Xiong, J., "CFD-Based Frequency Domain Method for Dynamic Stability Derivative Estimation with Application to Transonic Truss-Braced Wing," AIAA Aviation Forum, Applied Aerodynamics, AIAA-2022-3596, June 2022.

[5] Harrison, N. A., Hoffman, K., Lazzara, D. S., Reichenbach, E. Y., Sclafani, A. J., and Droney, C. K., "Subsonic Ultra Green Aircraft Research: Phase IV Final Report - Volume I Mach 0.80 Transonic Truss-Braced Wing High-Speed Design Report," NASA/CR-20220016017, October 2023.

[6] Theodorsen, T., "General Theory of Aerodynamic Instability and the mechanism of Flutter", NACA Report No. 496, 1949.

[7] Harrison, N. A., Gatlin, G. M., Viken, S. A., Breyar, M., Dickey, E. D., Hoffman, K., and Reichenbach, E. Y., "Development of an Efficient M=0.80 Transonic Truss-Braced Wing Aircraft," AIAA-2020-0011, January 2020.

[8] Xiong, J. and Nguyen, N., "Steady and Unsteady Simulations of Transonic Truss-Braced Wing Aircraft for Flight Dynamic Stability Analysis," AIAA Applied Aerodynamics Conference, June 2022.

[9] Nguyen, N. and Xiong, J., "Frequency Domain Method for Dynamic Control Derivative Estimation with Application to Transonic Truss-Braced Wing," AIAA Applied Aerodynamics Conference, AIAA-2023-3945, June 2023.

[10] Nguyen, N. and Xiong, J., "Nonlinear Dynamic Control Derivative Analysis for Aircraft Application to Transonic Truss-Braced Wing," AIAA Applied Aerodynamics Conference, AIAA-2024-0251, January 2024.